Design and Experimental Study of Turbine Blade Cooling Structure for an Engine

Jintao Jiang , Suyan Dong * , Rongxiao Dong , Zhisheng Wang , Yi Fu , Penghui Liu , Wei Fan

Posted Date: 6 August 2025

doi: 10.20944/preprints202508.0449.v1

Keywords: Turbine blade; Additive Manufacturing; Cooling structure; Film cooling; Cooling efficiency

 doi:10.20944/preprints202508.0449.v1

Article

Design and Experimental Study of Turbine Blade Cooling Structure for an Engine

Jintao JIANG [1], Suyan DONG [1,*], Rongxiao DONG [2], Zhisheng WANG [1], Yi FU [1], Penghui LIU [1] and Wei FAN [1]

[1] School of Power and Energy, Northwestern Polytechnical University, Xi'an 710029, China

[2] Science and Technology on Space Physics Laboratory, China Academy of Launch Vehicle Technology, Beijing 100076, China

* Correspondence: dsy@nwpu.edu.cn

Abstract

To address issues such as leading-edge and trailing-edge ablation and cracking of turbine blades during operation in an engine, this study integrates the characteristics of additive manufacturing technology and utilizes a comprehensive simulation and design platform for turbine cooled blades to design three schemes of film cooling structures. Numerical simulations were employed to optimize the blade cooling configurations, resulting in a finalized cooling structure scheme, which was then subjected to experimental evaluation of its cooling performance. An experimental platform for turbine blade cooling effectiveness was established, capable of simulating actual engine operating parameters. Based on this platform, experimental studies were conducted to investigate the effects of key parameters—including pressure ratio(β), temperature ratio(K), and flow ratio(B)-on the cooling effectiveness and the dimensionless temperature distribution on the blade surface. Experimental results show that within the studied operating conditions, the β has a greater impact on the cooling effectiveness of the blade compared to variations in B and K. When the β = 1.2, the cooling effectiveness of the blade surface is 0.130, and when β = 1.6, the effectiveness increases to 0.176, representing a 35.38% improvement. Within the tested range, variations in flow ratio resulted in a 19.12% increase in cooling effectiveness, while changes in temperature ratio led to a 26.62% improvement.

Keywords: turbine blade; additive manufacturing; cooling structure; film cooling; cooling efficiency

1. Introduction

With the continuous improvement of aero-engine performance, the temperature at the combustor exit has been steadily increasing[1], placing higher demands on the materials and cooling technologies of turbine blades due to the rising turbine inlet temperatures. The turbine inlet temperature of next-generation aero-engines is expected to reach 2400 K [2]. Such excessively high temperatures can lead to blade creep, cracking, and ablation, posing serious threats to engine operation. Therefore, in addition to improving the high-temperature resistance of materials, it is urgently necessary to implement effective enhanced cooling technologies for turbine blade cooling[3].

At present, turbine blade cooling technologies mainly include film cooling[4,5], impingement cooling[6,7], convective cooling [8,9], advanced cooling structures [10,11], and thermal barrier coating (TBC) technologies [12,13]. The optimization of these technologies requires consideration of multi-physics coupling mechanisms involving aerodynamics, heat transfer, and structural strength. Numerous experimental and numerical studies have been conducted by researchers worldwide to investigate the effects of cooling structure design and aerodynamic parameter variations on the overall cooling performance of turbine blades.

In terms of cooling structure design, Rao et al. [10] proposed the use of W-shaped ribs in multi-jet impingement cooling to enhance heat transfer performance. At a Reynolds number of 30,000, the

 doi:10.20944/preprints202508.0449.v1

W-shaped ribs increased the average impingement heat transfer area of the test plate by approximately 9.6%, with negligible additional pressure loss. Haydt et al. [14–17] systematically studied the geometric parameters of backward-expanded film cooling holes. Experimental results showed that increasing the lateral expansion angle, reducing the hole spacing, and enlarging the exit area significantly improved the spanwise-averaged film cooling effectiveness downstream, with a maximum improvement of up to 23%.

Regarding variations in aerodynamic parameters, Gao et al. [18] experimentally found that under moderate blowing ratio conditions (M = 0.9), the highest film cooling effectiveness was achieved near the hole region, while higher blowing ratios (M = 1.5) were required in the downstream region to maintain effective film coverage. Narzary et al. [19] investigated the effect of density ratio on film cooling of turbine blades through experiments. The results showed that as the density ratio increased, film cooling effectiveness improved over most regions of both the pressure and suction sides. Jeong et al. [20] experimentally studied the influence of density ratio and blowing ratio on film cooling effectiveness. The results indicated that under high blowing ratio conditions, the film cooling effectiveness near the leading edge increased with increasing density ratio.

As a critical component of aero-engines, the manufacturing quality of turbine blades directly influences their service life and operational stability [21]. These blades feature complex aerodynamic profiles, a high density of film cooling holes with small diameters, and non-linear hole distributions along the blade span, all of which significantly complicate the fabrication process. Traditional manufacturing methods, such as subtractive machining and electrochemical processing, face considerable limitations when dealing with such intricate geometries and fine structures [22–24].

Additive manufacturing (AM)[25–28], which builds components layer by layer, offers a promising solution by enabling near-net-shape fabrication of complex internal cooling structures. This technology achieves a dimensional accuracy on the order of 0.1 mm, reduces production lead times to less than two weeks, and improves material utilization by more than 40 percent. These advantages make AM particularly well suited for producing components with the geometric complexity and precision required in aerospace applications[29]. Given the intricate airfoil geometry, the small size of the film cooling holes, and the complex flow exit angles characteristic of turbine blades, this study selects additive manufacturing as the preferred fabrication approach for the experimental blade specimens.

In summary, most existing studies are based on similar principles [30] and are conducted under simplified experimental conditions, while experimental data on the cooling performance of turbine blades under real engine operating conditions remain insufficient. Therefore, in this study, three film cooling schemes were proposed based on the original turbine working blade, utilizing a turbine blade simulation and design platform [31]. By optimizing the number, angle, and arrangement of film cooling holes, an improved turbine blade model was developed.

To ensure the dimensional accuracy of the complex internal cooling channels and film holes, the experimental blades were fabricated using Selective Laser Melting (SLM) technology. Subsequently, a gas turbine blade cooling effectiveness test platform was established. This platform, which integrates a model combustor and a multi-stage air supply system, is capable of simulating the inlet temperature gradients and coolant-to-mainstream flow ratios characteristic of real aero-engine conditions. Using this platform, experimental studies were conducted to investigate the effects of flow ratio, temperature ratio, and pressure ratio on the thermal performance of turbine working blades. The findings provide both theoretical and engineering support for the thermal protection design of turbine blades.

2. Experimental System and Conditions

2.1. Experimental System

Figure 1 illustrated the schematic diagram of the experimental system for measuring the cooling effectiveness of turbine blades. The entire system consisted of a high-enthalpy air supply system, a

 doi:10.20944/preprints202508.0449.v1

kerosene supply system, a single-cup combustion chamber model, a secondary air supply system, a circulating cooling water system, a cascade test section, and a data acquisition system. The high-enthalpy air supply system was capable of continuously delivering air at a maximum flow rate of 3.0 kg/s and a maximum pressure of 5.5 MPa. The air source tank located upstream of the heater had a volume of 50 m^3, which ensured a stable and continuous air supply throughout the blade cooling effectiveness experiments.

The experimental procedure was as follows: Based on the required mainstream gas temperature, pressure, and flow rate under the turbine blade test conditions, the operating parameters for the high-enthalpy air heater and the combustor were calculated. The high-temperature gas by combustion flowed through a 1170.5 mm-long sector-shaped wind tunnel, where it fully developed before entering the cascade test section for the cooling effectiveness experiment. The secondary air supply system adopted a high-pressure air tapping scheme. After pressure stabilization and flow control through a valve assembly and flow controller, the air was heated to the required temperature by an electric air heater and then introduced into the interior of the turbine blade test article.

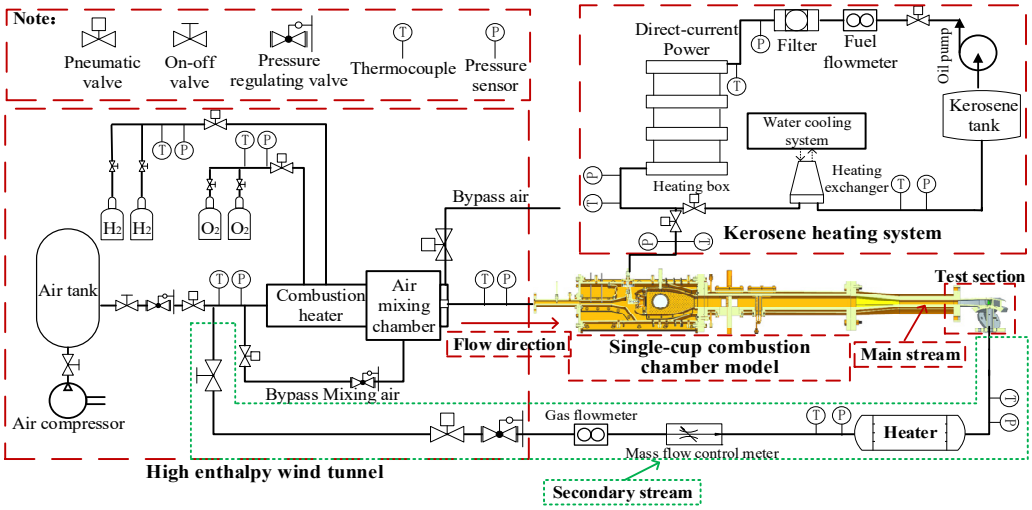

Figure 1. Schematic diagram of the experimental system.

2.2. Test Blade

Figure 2 showed the model of the turbine blade test section. The test section consisted of one experimental blade and two end-support (companion) blades, together forming two periodic sector-shaped cascades. The experimental blade was fabricated using additive manufacturing technology, with the nickel-based superalloy IN-738 selected as the blade material. This alloy had a maximum temperature resistance of up to 1173 K. The blade had a chord length of 19.94 mm, an overall height of 26.95 mm, and a minimum wall thickness of approximately 0.5 mm along the airfoil. The tenon (root) measured approximately 20 mm in length, and the total blade volume was 2089.6 mm^3.Thermocouples and pressure probes were installed 110 mm upstream of the cascade channel to measure the mainstream gas inlet temperature, total pressure, and static pressure.

Figure 2 also showed the schematic diagram of the thermocouple layout on the turbine blade surface. The measurement points were located at the 50% blade height cross-section, and their positions along the arc length of this section were indicated in the figure. A total of 16 K-type sheathed thermocouples with a diameter of 0.5 mm were embedded in the blade—7 on the pressure side and 9 on the suction side. To prevent any adverse effects on film cooling performance from directly welding thermocouples onto the blade surface, thermocouple mounting grooves were printed during the blade fabrication process. The thermocouples were then fixed into the grooves using laser welding. A coating made of the same material as the blade was sprayed onto the surface to fill the gap between the thermocouples and the grooves. The thinnest part of the coating above the embedded thermocouples was approximately 0.05 mm. The surface was carefully polished to ensure

 doi:10.20944/preprints202508.0449.v1

that the aerodynamic profile of the blade remained unchanged. The appearance of the blade after thermocouple embedding and coating is shown in **Figure 3**.

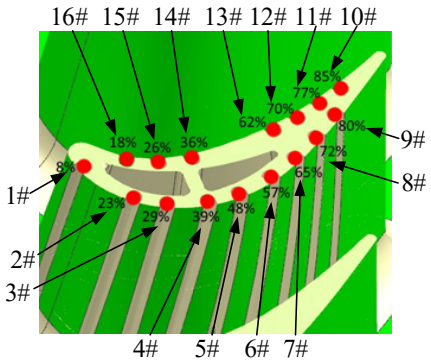

Figure 2. Schematic diagram of turbine blade measurement points.

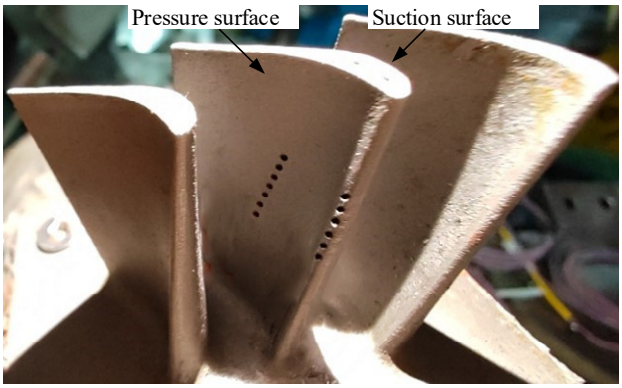

Figure 3. Photos of test blade with thermocouples.

2.3 Experimental Parameters and Definitions

The flow ratio is defined as:

$$B = m_c / m_g \tag{1}$$

Where, m_c is the secondary flow mass flow rate, and m_g is the mainstream gas mass flow rate.

The temperature ratio is defined as:

$$K = T_g / T_c \tag{2}$$

Where, T_c is the secondary flow temperature, and T_g is the mainstream gas temperature.

The gas pressure ratio is defined as:

$$\beta = \frac{p_{in}^*}{p_{out}} \tag{3}$$

Where, p_{in}^* is the cascade gas inlet total pressure, and p_{out} is the cascade gas outlet static pressure.

The dimensionless temperature on the blade surface is defined as:

$$\varepsilon = T_w / T_g \tag{4}$$

Where, T_w is the turbine blade surface temperature.

The cooling effectiveness of the blade is defined as:

$$\eta = \frac{T_g - T_w}{T_g - T_c} \tag{5}$$

The arc-length averaged cooling effectiveness of the turbine blade is defined as:

$$\eta_{ave} = \frac{1}{S}\int_0^s \eta ds = \frac{1}{S}\sum_{i=1}^{n} \Delta S_i \eta_i \tag{6}$$

Where, S is the total arc-length of the blade outer surface at the 50% span section, and ΔS_i is the arc-length corresponding to measurement point i.

 doi:10.20944/preprints202508.0449.v1

2.4 Experimental Uncertainty Analysis

The measurement parameters of the turbine blade, along with the ranges and accuracies of the instruments used in the experiment, are listed in **Table 1**. The experimental results primarily focused on investigating the cooling effectiveness (η) of the blade surface and the dimensionless temperature (ε) on the blade surface.

The η on the blade surface is defined as:

$$\frac{d\eta}{\eta}=\sqrt{\left(\frac{dT_g}{T_g}\right)^2+\left(\frac{dT_w}{T_w}\right)^2+\left(\frac{dT_c}{T_c}\right)^2} \tag{7}$$

Where, T_g, T_w, and T_c represent the mainstream gas temperature at the cascade inlet, the blade surface temperature, and the secondary air temperature, respectively. According to the standard error analysis method proposed by Moffat et al. [32], the uncertainties of the cooling effectiveness and the dimensionless surface temperature in this experiment had been 4.2% and 3.17%, respectively, indicating that the experimental measurements of the turbine blade's cooling performance in this study were reliable.

Table 1. Measurement parameters and instruments for the blade experiment.

Parameters	Measuring instrument	Range	Uncertain/%
Blade surface temperature	K thermocouple	273~1000 K	0.5
Total inlet/outlet temperature	K thermocouple	273~1000 K	0.5
Total inlet/outlet pressure	Pressure sensor A	0.5~1.5 MPa	0.5
Inlet/outlet static pressure	Pressure sensor B	0.1~5.0 MPa	0.5
Secondary flow	Mass flowmeter	0.1~100 g/s	1.0
	Mass flow control meter	0.1~5.0 g/s	0.05

3. Numerical Simulation

In this study, a fluid-structure coupled numerical simulation method was adopted. The Realizable *k-ε* turbulence model [33,34] was used, and the pressure-based segregated solver was employed. The discretization scheme for the governing equations utilized the third-order *QUICK* scheme. The pressure–velocity coupling was handled using the SIMPLEC algorithm, and the pressure interpolation was performed using the standard scheme. Pressure, momentum, turbulent kinetic energy, and energy equations were all discretized with second-order accuracy. The average temperature variation on the blade surface during the final 1000 iterations was less than 0.08%.

3.1. Computational Model and Boundary Conditions

Figure 4 shows the original turbine blade model of a certain type of engine, in which no cooling hole structure was designed. The computational model and boundary conditions are illustrated in **Figure 5**. To prevent backflow at the inlet and outlet of the fluid domain during the simulation, which could affect the stability of the calculation, the gas inlet and outlet regions were appropriately extended.

 doi:10.20944/preprints202508.0449.v1

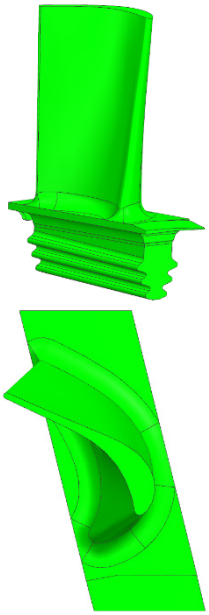

Figure 4. Original turbine blade model.

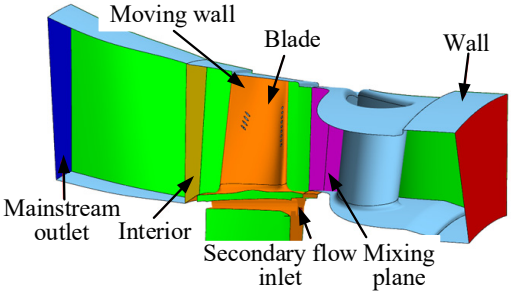

Figure 5. Computational domain and boundary conditions of turbine blade calculation.

3.2. Mesh

The gas passage, blade cascade passage, and secondary air passage were defined as the fluid domain, while the blade airfoil and blade tenon were defined as the solid domain. The mesh division is shown in Figure 6. To better capture the flow and heat transfer details near the wall surfaces, boundary layer meshes were applied in regions of the fluid domain adjacent to the solid walls, with a total of five layers and the first layer corresponding to $y^+ < 1$. In regions with steep parameter gradients, such as around the film cooling holes and the leading edge, mesh refinement was applied. The total number of mesh elements in the solid domain of the blade was 800,000, while the fluid domain contained 4.2 million elements.

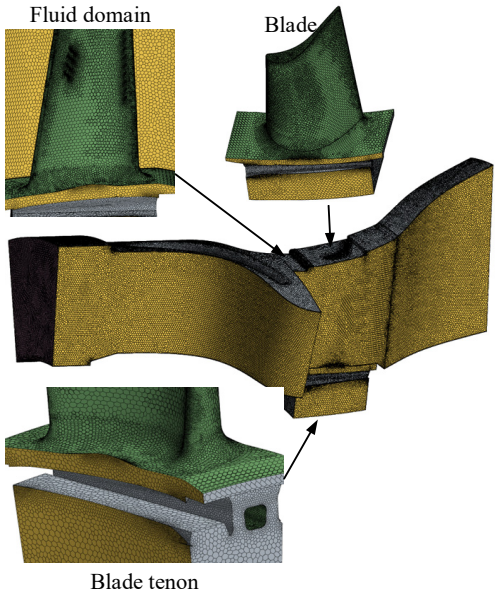

Figure 6. Computational domain and grid.

 doi:10.20944/preprints202508.0449.v1

3.3. Mesh Independence

Numerical simulations were carried out using the original turbine blade structure as an example, and a grid independence verification process was conducted. The results of the grid independence study are presented in **Table 2**.

Five sets of meshes with different densities, ranging from 1 million to 9 million elements, were used to evaluate the sensitivity of the simulation results to grid resolution. When the mesh count increased from 1 million to 5 million, the change in the average temperature of the blade airfoil and tenon became less than 0.5%. Therefore, a mesh containing 5 million elements was ultimately selected for subsequent simulations, and this mesh resolution was used for the grid generation of blades with different cooling structure designs.

Table 2. Gird independence validation.

Mesh/10^6	1.0	3.0	5.0	9.0
Average blade temperature/K	1018.9	1024.8	1025.3	1025.6

3.4. Numerical Calculation Conditions

At the engine design point, the flow ratio was 1.0% (with p_c = 0.8 MPa), the temperature ratio was 1.46, and the pressure ratio of the hot gas was 1.41. **Table 3** presents the operating conditions used in the numerical simulations. In the table, p_{in}^* represents the total pressure at the inlet of the mainstream high-temperature gas, T_g is the inlet temperature of the mainstream gas, m_g is the mainstream gas mass flow rate, p_c is the total pressure at the secondary air inlet, and T_c is the secondary air temperature.

During the numerical simulation, the inlet temperature T_g was set to 1286.4 K. A User-Defined Function (UDF) was used to define the gas inlet boundary conditions, and the temperature non-uniformity coefficient at the gas inlet was set to 0.2.

Table 3. Calculation conditions.

Parameters	Value
p_{in}^*	1.34 MPa
T_g	1284.6 K
m_g	0.585 kg/s
p_c	0.8 MPa
T_c	708.5 K

3.5. Validation of the Simulation Results

Figure 7 shows the comparison between the experimental and simulated dimensionless temperature distribution curves on the blade surface. Both the experimental and numerical conditions correspond to the engine design point. The temperature data were obtained at 16 measurement points located along the 50% blade height cross-section, with each value representing the average temperature within a φ = 0.6 mm area around the measurement point.

The experimental data and simulation results showed good overall agreement in terms of trend. The maximum deviation between the simulation and experimental results was 9.65%, while the minimum deviation was 2.59%.

The discrepancies between the experimental and simulation results were mainly attributed to the following factors:

(1) Local deviations between the actual thermocouple installation locations and the mesh nodes in the simulation caused a mismatch between the measured and computed temperatures;

(2) In the numerical simulation, the prescribed state of the mainstream gas in the turbine blade passage may have differed from the actual gas conditions in the experiment;

 doi:10.20944/preprints202508.0449.v1

(3) The thermocouple installation and coating process on the blade surface may have introduced measurement errors, leading to discrepancies between the actual and simulated temperature values.

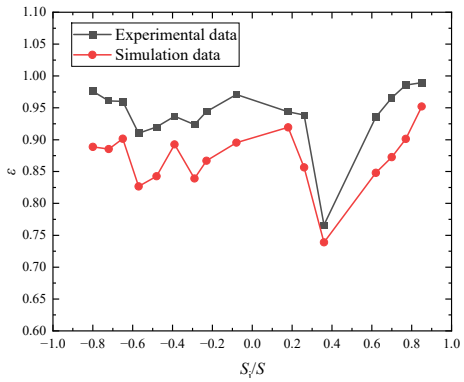

Figure 7. Comparison of simulation and experimental data.

4. Numerical Results and Discussion

4.1. Temperature Field of the Original Turbine Blade

Figure 8 shows the surface temperature distribution contour of the original turbine blade under the engine design point conditions. From the figure, four main high-temperature regions and two secondary high-temperature regions near the blade tip can be observed on the blade surface. The main high-temperature areas are primarily concentrated along the leading edge and trailing edge within the 40% to 80% blade height range. The highest temperature in the leading-edge hot region reaches 1154 K, while the trailing-edge hot region peaks at 1145 K. The secondary high-temperature areas near the blade tip reach a maximum of 1096 K, and the average temperature of the blade airfoil and tenon is 1025.3 K.

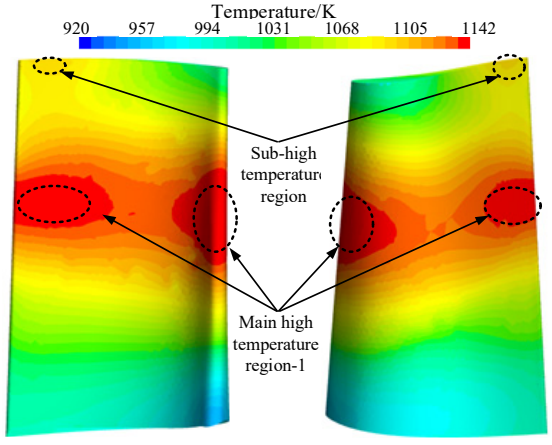

Figure 8. Surface temperature distribution of turbine blade.

The reason for this distribution is that the original turbine blade was designed without film cooling structures and is therefore a solid blade. The formation of high-temperature regions on the blade surface essentially results from the coupled effects of fluid flow and heat transfer. The high-temperature gas enters the working blade passage from the turbine guide vanes, and the flow state and heat transfer characteristics between the turbine guide vanes and working blades determine that the high-temperature zones are concentrated in the mid-span region of the blade. The temperature distribution characteristics of the blade's high-temperature areas correspond closely with those of the combustor outlet.

 doi:10.20944/preprints202508.0449.v1

The original turbine blade material is the nickel-based superalloy IN-738, which has a maximum temperature resistance of approximately 1173 K. Since the highest temperatures in the leading and trailing edge hot regions approach the material's temperature limit, it is necessary to design cooling structures for the turbine blade to ensure its normal operation.

4.2. Design of the Blade Film Cooling Structure

Based on the temperature field analysis of the original turbine blade in the previous section, film cooling holes should be arranged near the blade leading edge and trailing edge to reduce the temperature in the high-temperature regions. Additionally, since the main high-temperature areas are concentrated within the 40% to 80% blade height range along the leading and trailing edges, the cooling structure design incorporates a denser distribution of film cooling holes in this region.

The original turbine blade has a solid structure without any film cooling holes. According to the distribution characteristics of the high-temperature regions described above, the turbine blade cooling structure was optimized using a comprehensive simulation and design platform for turbine cooled blades. Three targeted film cooling structure designs were proposed. Tables 4 and 5 present the specific parameters of these three cooling structure schemes, while Table 6 shows the turbine blade models and internal cooling channel layouts for Schemes 1 to 3.

Compared to Scheme 1, Scheme 2 increased the number of trailing edge film cooling holes and modified the discharge angles of the film holes at the leading edge and blade tip, as well as the dimensions of the internal cooling channels. Compared to Scheme 2, Scheme 3 reduced the number of film cooling holes at the leading edge and blade tip and adjusted the discharge angles of the film holes at the leading and trailing edges.

Table 4. Number of film cooling holes and parameters of internal cooling channels.

Position	Scheme 1	Scheme 2	Scheme 3
Leading Edge	9	9	6
Trailing Edge	4	5	5
Blade tip	2	2	1
Blade internal cooling channel	2.2×2.0 mm	2.2×1.5 mm	2.2×1.5 mm

Table 5. Film cooling hole angle.

Position	Scheme 1	Scheme 2	Scheme 3
Leading Edge	41°	39°	35°
Trailing Edge	30°	30°	45°
Blade tip	90°	88°	88°

Table 6. Model of cooling structure.

Scheme	Blade	Blade internal cooling passage
1		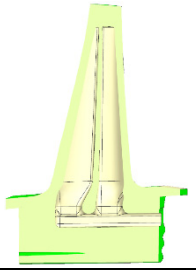

 doi:10.20944/preprints202508.0449.v1

2	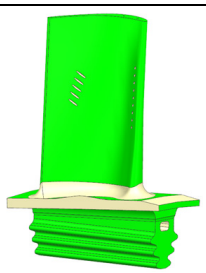	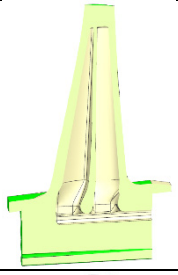
3	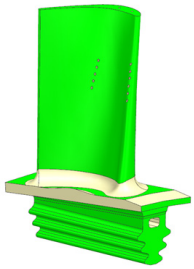	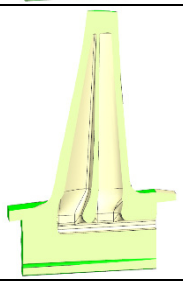

Figure 9 shows the definition of the film cooling hole orientation. The exit point *O* of the film cooling hole is defined as the intersection of the hole's central axis and the blade surface. A local reference coordinate system is established with point *O* as the origin: the surface normal direction is defined as the Z-axis, the tangential direction along the blade height as the Y-axis, and the tangential direction along the flow direction as the X-axis.

Reference plane A is defined as the XZ plane, and reference plane B as the YZ plane. The film cooling hole angle is defined as the angle between the central axis of the cooling hole and the XY plane.

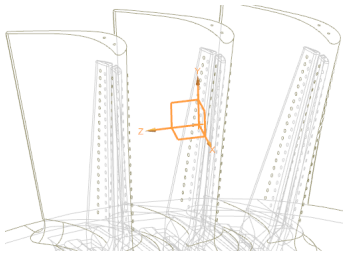

Figure 9. Schematic diagram of film cooling hole angle.

4.3. Surface Temperature Distribution of the Blade

Figure 10 presents the surface temperature distribution contours of the turbine blade under design-point conditions for Schemes 1 to 3, while **Table 7** compares the blade temperature and aerodynamic performance parameters for the three schemes. Compared with the original turbine blade temperature distribution shown in **Figure 8**, the incorporation of cooling structures in Schemes 1 to 3 effectively reduced the surface temperature and decreased the area of high-temperature regions on the blade.

In Scheme 1, film cooling holes were arranged along the blade leading edge, trailing edge, and tip. The combined effects of convective heat transfer from the coolant jets and the film isolation effect effectively reduced the blade surface temperature. Compared to the original turbine blade, the maximum temperature at the leading edge decreased by 5.74%. However, due to the relatively large outlet angle (41°) of the leading-edge film cooling holes, the film coverage was weakened, resulting in insufficient coolant coverage over the trailing-edge tip region. Consequently, the maximum temperature in the blade tip high-temperature region was 1083 K, only 1.19% lower than that of the original blade.

The presence of film cooling holes at the trailing edge in Scheme 1 helped reduce the area of high-temperature regions at the trailing edge, with the maximum temperature dropping by 7.83%. Meanwhile, the implementation of the cooling structure significantly lowered the average

 doi:10.20944/preprints202508.0449.v1

temperature of the blade body and root, which decreased by 13.14% compared to the original turbine blade.

The total cooling airflow through the film cooling holes of a single blade in Scheme 1 was 4.57 g/s. Compared to the original solid blade without cooling structures, the increased secondary cooling airflow led to greater aerodynamic losses. Therefore, it is necessary to comprehensively evaluate the trade-off between the secondary airflow consumption and the blade cooling effectiveness to propose an optimal cooling structure design.

To address the issues of large total cooling airflow and the large outlet angle of the leading-edge film holes in Scheme 1, Scheme 2 reduces the leading-edge film hole angle to 39° and increases the number of trailing-edge film holes, aiming to optimize the temperature characteristics of the trailing edge and the trailing-edge tip high-temperature region. Additionally, the internal cooling channel dimensions were reduced, lowering the total cooling airflow to 3.47 g/s.

In Scheme 2, the maximum temperature at the leading edge is 1082.4 K, which is similar to that of Scheme 1. However, the high-temperature region at the trailing edge shifts closer to the trailing-edge tip, located around 75–80% of the blade height. The maximum temperature in the trailing-edge high-temperature region decreases by 6.57% compared to Scheme 1. Furthermore, the high-temperature area at the trailing-edge tip is reduced, with its maximum temperature lowered by 4.79% relative to Scheme 1. Due to the reduced cooling airflow, the average temperature of the blade body and root increased by 0.34% compared to Scheme 1.

By modifying the blade's cooling structure, Scheme 2 significantly improves the blade's temperature distribution. The maximum temperatures remain within the material's allowable range. However, the total cooling airflow per blade is still 3.47 g/s, which, although reduced, still causes a degree of aerodynamic loss compared to the original turbine blade.

To further reduce the total secondary cooling airflow, Scheme 3 decreases the number of film cooling holes and modifies the outlet angles of both the leading- and trailing-edge holes to enhance coolant coverage efficiency. Compared to Scheme 2, Scheme 3's maximum leading-edge temperature is 1018.0 K, a 5.95% reduction. The high-temperature region distribution at the trailing edge is similar to that of Scheme 1, but its maximum temperature is 11.39% higher than in Scheme 2, and the high-temperature area is also enlarged. Due to the further reduction in the number of film cooling holes, the trailing-edge tip high-temperature area expands, and its maximum temperature increases by 1.68% compared to Scheme 2—though it still remains lower than in Scheme 1.

Meanwhile, the further reduction in cooling airflow in Scheme 3 leads to a 0.99% increase in the average temperature of the blade body and root compared to Scheme 2.

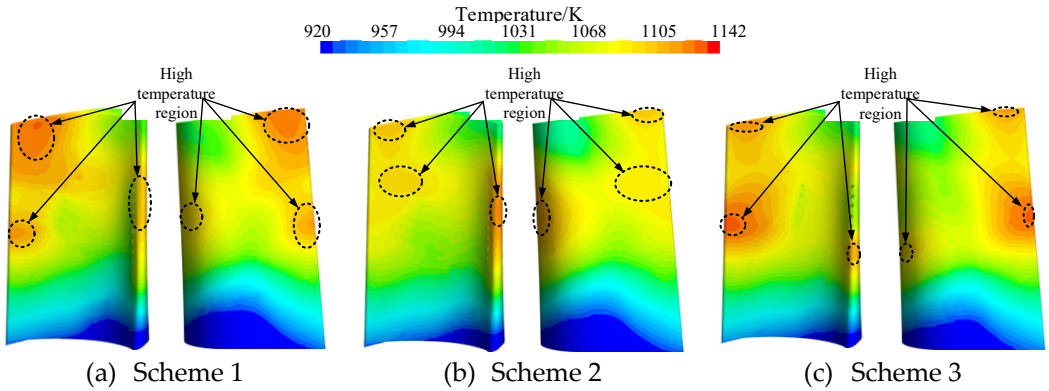

Figure 10. Temperature distribution of turbine blade surface

 doi:10.20944/preprints202508.0449.v1

Table 7. Parameter comparison of schemes 1~3.

Scheme	Maximum temperature on the surface of turbine blade/K	Average temperature of blade body and tenon/K	Total cooling air flow/g•s^{-1}
1	1087.8	890.6	4.57
2	1082.4	893.2	3.47
3	1098.3	902.4	2.00

4.4 Film Hole Flowline Distribution Characteristics

Figure 11 shows the flowline distribution diagrams of blade film hole outflow under design-point conditions for Engine Schemes 1–3. As shown in the figure, the cooling air jets in Scheme 1 exhibit poor wall-attachment performance, resulting in jet detachment and horseshoe vortex formation. The cooling airflow is biased toward the blade tip, leading to insufficient coverage in the trailing edge region and a relatively large high-temperature area near the trailing edge tip. Additionally, some streamlines bypass the blade tip, further weakening the cooling effectiveness.

To address the poor wall-attachment performance of the film hole outflow in Scheme 1, Scheme 2 reduces the front-edge outflow angle to 39°, while adjusting the internal cooling channel dimensions and increasing the number of film holes. The total cooling air mass flow rate is reduced to 3.47 g/s, enhancing the wall-adherence effect and further improving blade cooling performance. However, the outflow streamlines from the front-edge film holes still show partial flow bypassing the blade tip, resulting in localized small-scale vortex remnants, which are not favorable for efficient utilization of the cooling air.

Compared to Scheme 2, Scheme 3 further optimizes the front-edge film hole outflow angle. The outflow streamlines from the front-edge film holes directly target the suction surface and exhibit a parallel laminar pattern. The film coverage is improved, and the streamline attachment performance is significantly better than in the previous two schemes.

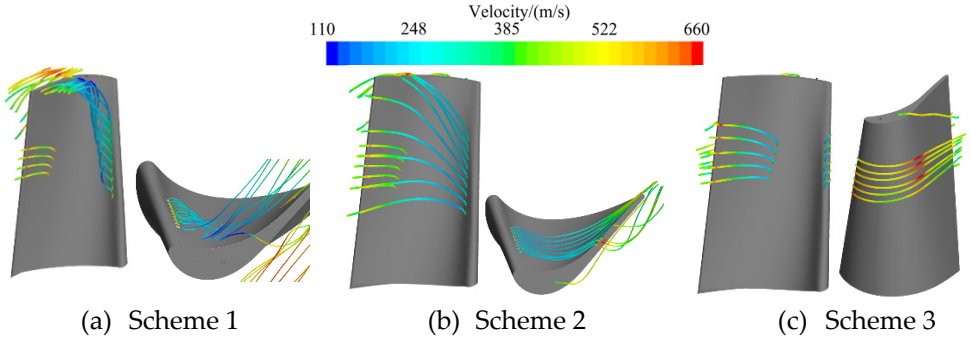

(a) Scheme 1 (b) Scheme 2 (c) Scheme 3

Figure 11. Temperature distribution of turbine blade surface

4.5. Final Experimental Blade Scheme

Based on the analyses in Sections 4.3 and 4.4, Scheme 3 significantly improves the cooling air coverage efficiency by adjusting the arrangement and angles of the film cooling holes. Under a relatively low total cooling air mass flow rate, it effectively enhances the surface temperature characteristics of the turbine blade. Compared to the original turbine blade, Scheme 3 reduces the blade surface maximum temperature to 1180 K, a decrease of 12.90%, and the average temperature of the blade body and tenon to 902.0 K, a decrease of 12.03%. Overall, all temperatures remain below the thermal limit of the IN-738 alloy (1173 K). The total cooling air mass flow rate in Scheme 3 is 2.0 g/s, representing reductions of 56.24% and 43.98% compared to Schemes 1 and 2, respectively, resulting in minimal aerodynamic loss of the blade. With the lowest cooling cost, Scheme 3 achieves efficient thermal protection and is therefore selected as the final optimized scheme for further experimental investigation on blade overall cooling efficiency.

 doi:10.20944/preprints202508.0449.v1

5. Experimental Results and Analysis

According to the actual operating conditions of the original turbine blade, the design point flow ratio is 1.0%, the temperature ratio is 1.46, and the total pressure ratio of the combustion gas is 1.41. The specific experimental conditions for the optimized turbine blade are shown in **Table 8**. The gas inlet temperature distribution follows the same pattern as the simulation results, with a temperature distribution factor of 0.2. During the experiment, variations in the flow ratio and temperature ratio are achieved by adjusting the secondary air flow rate and temperature, while changes in the total pressure ratio are controlled by adjusting the mainstream gas flow rate.

Table 8. Turbine blade experimental conditions.

Parameter	Value
B	0.8%，1.0%，1.2%
K	1.25，1.35，1.45，1.55，1.65
β	1.2，1.3，1.41，1.5，1.6

5.1 Effect of B on Cooling Performance

Figure 12 presents the dimensionless temperature distribution and cooling efficiency of the turbine rotor blade at different flow ratios under conditions of a temperature ratio of 1.2 and a pressure ratio of 1.41. In the figure, the horizontal axis represents the dimensionless length along the mid-section of the blade, with the blade leading edge as the origin. The negative X-axis direction corresponds to the suction side, and the positive X-axis direction corresponds to the pressure side.

As the B increases, the dimensionless surface temperature of the blade gradually decreases, while the cooling efficiency improves. This is because the increased secondary air flow enhances the film coverage on the blade surface, effectively isolating the hot gas from the external wall of the blade and suppressing convective heat transfer. Simultaneously, the internal cooling channels experience stronger convective heat transfer between the cooling air and channel walls, further reducing the blade surface temperature and improving cooling efficiency.

The cooling efficiency on the pressure side of the blade is higher than that on the suction side. When the B is 0.8%, the average dimensionless temperature on the pressure side is 0.924 with an average cooling efficiency of 0.171, while the average dimensionless temperature on the suction side is 0.940 with an average cooling efficiency of 0.146. When the B increases to 1.2%, the dimensionless temperature decreases by 1.70%, and the average cooling efficiency increases by 14.60%.

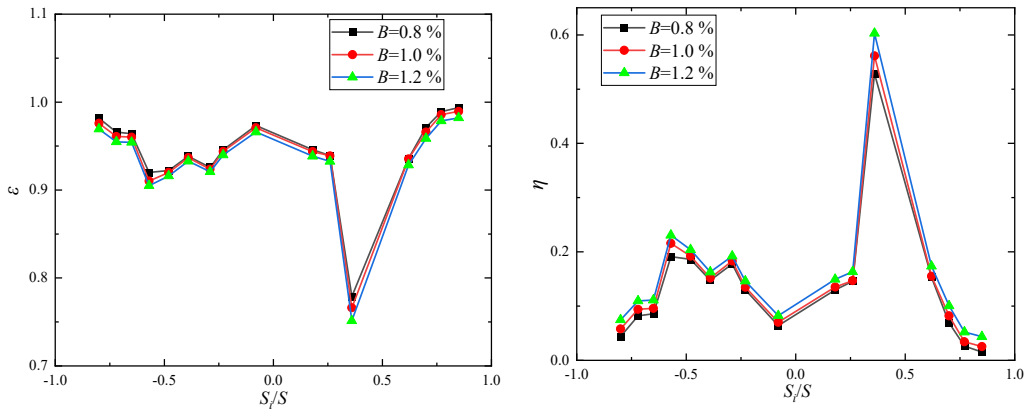

(a) Dimensionless temperature (b) Cooling efficiency

Figure 12. Effect of B on turbine blade cooling performance

 doi:10.20944/preprints202508.0449.v1

Figure 13 shows the blade cooling efficiency averaged along the arc length as a function of the flow ratio. As the *B* increases, the cooling efficiency gradually improves. When the *B* increases from 0.8% to 1.2%, the blade surface cooling efficiency rises from 0.136 to 0.162, an increase of 19.12%.

Although increasing the secondary air flow ratio can effectively enhance the blade cooling efficiency, it can also cause part of the air to lose its cooling effectiveness and result in greater aerodynamic losses. Therefore, reasonably adjusting the secondary air flow is crucial for improving the overall cooling efficiency of the blade.

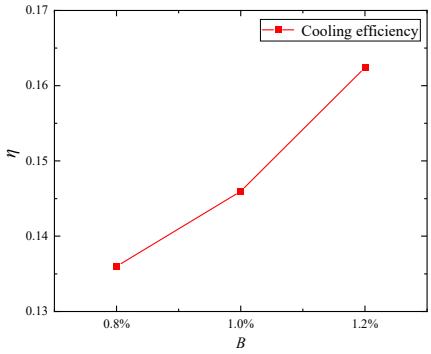

Figure 13. Variation curve of blade cooling efficiency with *B*.

5.2 Effect of K on Cooling Performance

Figure 14 shows the dimensionless surface temperature distribution and cooling efficiency variations of the turbine rotor blade under a cooling air flow ratio of 1.0% and a pressure ratio of 1.41 at different temperature ratios. As the temperature ratio increases, the dimensionless surface temperature of the blade gradually decreases, and the cooling efficiency correspondingly increases.

The reason is that, with an increase in *K*, the secondary air temperature decreases, which increases the cooling air's heat absorption capacity, thereby enhancing the blade's cooling efficiency. Within the experimental operating range, the cooling efficiency on the blade pressure side is higher than that on the suction side. When the *K* equals 1.65, the average dimensionless temperature on the pressure side is 0.915, with an average cooling efficiency of 0.189; on the suction side, the average dimensionless temperature is 0.926, with an average cooling efficiency of 0.165. Compared to the condition at *K* = 1.25, the dimensionless temperature decreased by 1.19%, and the average cooling efficiency increased by 14.55%.

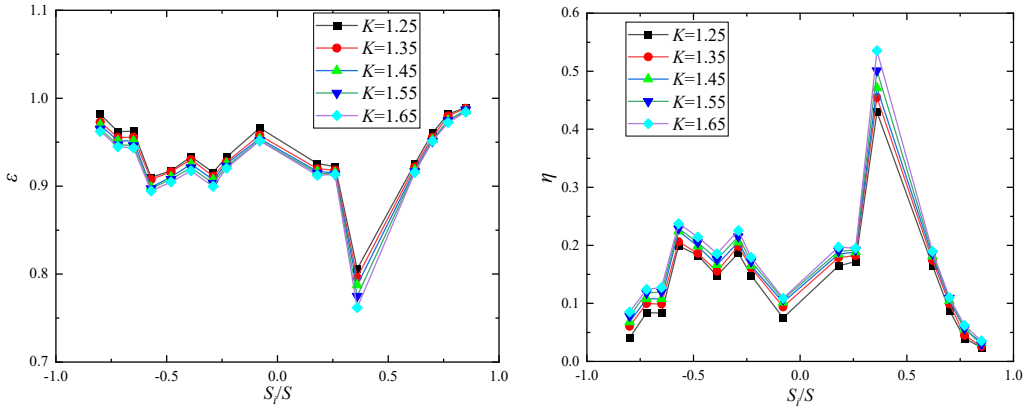

(a) Dimensionless temperature (b) Cooling efficiency

Figure 14. Effect of *K* on turbine blade cooling performance

 doi:10.20944/preprints202508.0449.v1

Figure 15 shows the variation of blade cooling efficiency under different mainstream-to-secondary flow temperature ratios. As the temperature ratio increases, the blade cooling efficiency gradually rises. When K = 1.25, the blade cooling efficiency is 0.139; when K = 1.65, it increases to 0.176, representing an improvement of 26.62%.

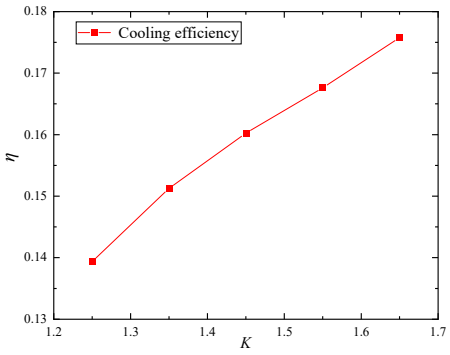

Figure 15. Variation curve of blade cooling efficiency with *K*.

5.3. Effect of β on Cooling Performance

Figure 16 shows the dimensionless surface temperature distribution and cooling efficiency variations of the turbine rotor blade under a cooling air flow ratio of 1.0% and a temperature ratio of 1.46 at different pressure ratios. During the experiment, changes in the pressure ratio were achieved by adjusting the mainstream gas flow rate, while maintaining consistent flow and temperature ratios between the mainstream gas and the secondary cooling air.

As the β increases, the dimensionless surface temperature of the blade gradually decreases, and the cooling efficiency correspondingly increases. The effects of β on blade cooling performance are similar to those of flow ratio and temperature ratio. The cooling efficiency on the pressure side of the blade is higher than that on the suction side. When β increases from 1.2 to 1.6, the dimensionless temperature on the pressure side decreases by 2.33%, and the average cooling efficiency increases by 43.41%; on the suction side, the dimensionless temperature decreases by 1.48%, and the average cooling efficiency increases by 28.24%.

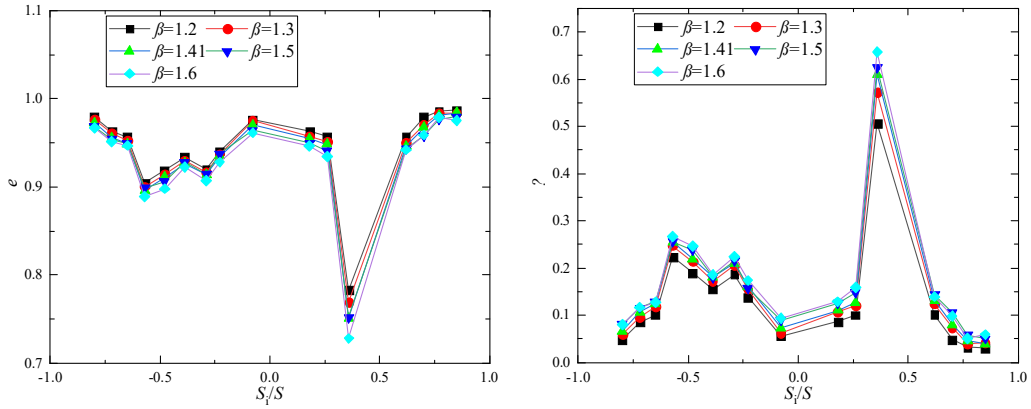

(a) Dimensionless temperature (b) Cooling efficiency

Figure 16. Effect of β on turbine blade cooling performance

Figure 17 shows the variation of the cooling efficiency on the blade surface with respect to the β. As the β increases, the cooling efficiency on the blade surface gradually rises. When the β is 1.2, the cooling efficiency is 0.130; when β increases to 1.6, the cooling efficiency reaches 0.176, representing an increase of 35.38%.

 doi:10.20944/preprints202508.0449.v1

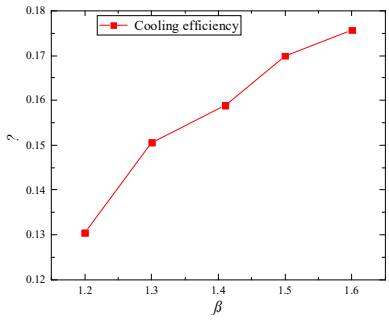

Figure 17. Variation curve of blade cooling efficiency with β.

6. Conclusions

Based on the conducted study, the following conclusions were drawn:

1) Within the experimental conditions, as the mass flow ratio increases, the cooling efficiency gradually improves. When the mass flow ratio increases from 0.8% to 1.2%, the overall cooling efficiency on the blade surface rises from 0.136 to 0.162, representing a 19.12% improvement. However, the increase in flow ratio has no significant effect on the distribution of surface cooling efficiency or the dimensionless temperature distribution on the blade surface. Since the variation range of secondary flow in this study is relatively small, the influence of the mass flow ratio on overall cooling efficiency is limited.
2) With an increase in the temperature ratio between the secondary flow and the mainstream gas, the overall cooling efficiency of the blade increases. When the temperature ratio K = 1.25, the cooling efficiency is 0.139; when K = 1.65, the efficiency reaches 0.176, indicating an increase of 26.62%.
3) The pressure ratio has a greater influence on the blade's overall cooling efficiency compared to the mass flow and temperature ratios. When the pressure ratio β = 1.2, the cooling efficiency of the blade surface is 0.130, while at β = 1.6, it increases to 0.176, representing a 35.38% improvement.
4) The cooling structure of the turbine blade was optimized based on numerical simulation methods and manufactured using additive manufacturing technology. Experimental results show that the blade's overall cooling performance meets the design requirements.

Author Contributions: Conceptualization, J.J. and D.S.; methodology, J.J. and D.S.; software, J.J., and D.S.; validation, J.J., D.S. and R.D.; formal analysis, J.J. and Z.W; investigation, J.J.; resources, J.J., and F.Y.; data curation, D.S. and R.D., and P.L.; writing—original draft preparation, J.J.; writing—review and editing, D.S., and R.D.; visualization, W.F.; supervision, W.F., and D.S.; project administration, W.F., and D.S., and D.S.; funding acquisition, W.F. All authors have read and agreed to the published version of the manuscript.

Funding: Please add: This research was funded by the Key Project of the National Natural Science Foundation of China (No. 52336006).

Data Availability Statement: Data are contained within the article

Conflicts of Interest: The authors declare no conflict of interest.

Abbreviations

The following abbreviations are used in this manuscript:

β	Pressure ratio
K	Temperature ratio
B	Flow ratio
TBC	Thermal barrier coating technology
m_c	Secondary flow mass flow rate
m_g	Mainstream gas mass flow rate

 doi:10.20944/preprints202508.0449.v1

T_c	Secondary flow temperature
T_g	Mainstream gas temperature
pc	Total pressure at the secondary air inlet
p_{in}^*	Cascade gas inlet total pressure
p_{out}	Cascade gas outlet static pressure
T_w	Turbine blade surface temperature
S	Total arc-length of the blade outer surface at the 50% span section
ΔS_i	Arc-length corresponding to measurement point i
ε	Blade surface dimensionless temperature
η	Cooling effectiveness

References

1. Kong, X., Zhang, Z, Zhu, J., et al. Research Progress on Cooling Structure of Aeroengine Air-Cooled Turbine Blade. *Journal of Propulsion Technology*, **2022**, *43*, 6-28. https://doi.org/10.13675/j.cnki.tjjs.200632
2. Zeng, Q., Chen, X. Combustor Technology of High Temperature Rise for Aero Engine. *Progress in Aerospace Sciences*. **2023**, 140. 100927. https://doi.org/10.1016/j.paerosci.2023.100927
3. Nourin, F. N., Amano, R. S. Review of Gas Turbine Internal Cooling Improvement Technology. *Journal of Energy Resources Technology*. **2020**, *143*, 080801. https://doi.org/10.1115/1.4048865
4. Zhu, H., Xie, G., Zhu, R., et al. Comparisons on Flow Characteristics and Film Cooling Performance of Cylindrical and Sister Holes with/without internal coolant crossflow. *International Journal of Thermal Sciences*. **2022**, *182*, 107791. https://doi.org/10.1016/j.ijthermalsci.2022.107791
5. Ye, L., Liu, C. l., Liu, H. y., et al. Experimental and Numerical Study on the Effects of Rib Orientation Angle on Film Cooling Performance of Compound Angle Holes. *International Journal of Heat and Mass Transfer*. **2018**, *126*, 1099-1112. https://doi.org/10.1016/j.ijheatmasstransfer.2018.06.064
6. Chen, G., Liu, Y., Rao, Y., et al. Numerical Investigation on Conjugate Heat transfer of Impingement/Effusion Double-wall Cooling with Different Crossflow Schemes. *Applied Thermal Engineering*. **2019**, *155*, 515-524. https://doi.org/10.1016/j.applthermaleng.2019.04.019
7. Zhang, M., Wang, N., Han, J. C. Internal Heat Transfer of Film-cooled Leading Edge Model with Normal and Tangential Impinging Jets. *International Journal of Heat and Mass Transfer*. **2019**, 139, 193-204. https://doi.org/10.1016/j.ijheatmasstransfer.2019.04.140
8. Zhang, M., Wang, N., and Han, J. C. Overall Effectiveness of Film-cooled Leading Edge Model with Normal and Tangential Impinging Jets. *International Journal of Heat and Mass Transfer*. **2019**, *139*, 577-587. https://doi.org/10.1016/j.ijheatmasstransfer.2019.05.037
9. Jia, G., Zhang L., Lu C., et al. Film Cooling Performance with Internal Coolant Channel Crossflow. *Journal of Aerospace Power*. **2015**, *30*, 823-830. https://doi.org/10.13224/j.cnki.jasp.2015.04.008
10. Rao, Y., Chen, P., Wan, C. Experimental and Numerical Investigation of Impingement Heat Transfer on the Surface with Micro W-shaped Ribs. *International Journal of Heat and Mass Transfer*. **2016**, *93*, 683-694. https://doi.org/10.1016/j.ijheatmasstransfer.2015.10.022
11. Kalghatgi, P., Acharya, S. Flow Dynamics of a Film Cooling Jet Issued From a Round Hole Embedded in Contoured Crate. *Journal of Turbomachinery*, **2019**, *141*, 081006. https://doi.org/10.1115/1.4043071
12. Zhang, Z.; Zeng, W.; Bian, X., et al. Effects of Thermal Barrier Coating on Temperature and Stress of Turbine Rotor Blade. *Journal of Propulsion Technology*. **2023**, *5*, 218-231. https://doi.org/10.13675/j.cnki.tjjs.2204035
13. Zhu, J., Zhao, C., Qiu, L. Thermal Protection Effectiveness of Thermal Barrier Coatings in Turbine Blade Applications. *Journal of Aerospace Power*. **2019**, *34*, 2503-2508. https://doi.org/10.13224/j.cnki.jasp.2019.11.022
14. Haydt, S., Lynch, S. Cooling Effectiveness for a Shaped Film Cooling Hole at a Range of Compound Angles. *Journal of Turbomachinery*, **2019**, *141*, 041005. https://doi.org/10.1115/1.4041603
15. Haydt, S., Lynch, S. Flowfield of a Shaped Film Cooling Hole Over a Range of Compound Angles. *ASME Turbo Expo 2018: Turbomachinery Technical Conference and Exposition*, Oslo, Norway, June 11–15, **2018**, GT2018-75728. https://doi.org/10.1115/GT2018-75728
16. Haydt, S., Lynch, S., Lewis, S. The Effect of a Meter-Diffuser Offset on Shaped Film Cooling Hole Adiabatic Effectiveness. *Journal of Turbomachinery*. **2017**, *139*, 091012. https://doi.org/10.1115/1.4036199

 doi:10.20944/preprints202508.0449.v1

17. Haydt, S., Lynch, S., Lewis, S. The Effect of Area Ratio Change Via Increased Hole Length for Shaped Film Cooling Holes With Constant Expansion Angles. *Journal of Turbomachinery*. **2018**, *140*, 051002. https://doi.org/10.1115/1.4038871
18. Gao, Z., Narzary, D. P., Han, J.C. Film Cooling on a Gas Turbine Blade Pressure Side or Suction Side with Axial Shaped Holes. *International Journal of Heat and Mass Transfer*. **2008**, *51*, 2139-2152. https://doi.org/10.1016/j.ijheatmasstransfer.2007.11.010
19. Narzary, D. P., Liu, K. C., Rallabandi, A. P., et al. Influence of Coolant Density on Turbine Blade Film-Cooling Using Pressure Sensitive Paint Technique. *Journal of Turbomachinery*. **2011**, *134*, 895-908. https://doi.org/10.1016/j.ijheatmasstransfer.2017.08.020
20. Jeong, J. Y., Kwak, J. S., Park, J. S., et al. Measurement of Film Cooling Effectiveness for the First-Stage Vane and Endwall of a Gas Turbine With Fan-Shaped Holes. *ASME Turbo Expo 2017: Turbomachinery Technical Conference and Exposition*. Charlotte, North Carolina, USA. June 26–30, **2017**. GT2017-63896. https://doi.org/10.1115/GT2017-63896
21. Zhang, X. Application of Metal Additive Manufacturing in Aero-engine. *Journal of Aerospace Power*, **2016**, *31*, 10-16. https://doi.org/10.13224/j.cnki.jasp.2016.01.002
22. Yu, Z., Guo, Y., Sun, H., et al. Recent Progress in Structural Integrity of Novel Materials and Advanced Techniques. *Acta Aeronautica et Astronautica Sinica*. **2024**, 45, 29888. https://doi.org/10.7527/S1000-6893.2024.29888
23. Zhang, X., Tao, C., Liu, C., et al. Investigation of Processing Methods and Development of Gas Holes of Engine Blade. *Materials Reports*. **2013**, *27*, 117-120. https://doi.org/10.3969/j.issn.1005-023X.2013.21.024
24. Sambhav, K., Tandon, P., Kapoor, S. G., et al. Mathematical Modeling of Cutting Forces in Microdrilling. *Journal of Manufacturing Science and Engineering*. **2013**, *135*, 014501. https://doi.org/10.1115/1.4007955
25. Peng, L., Taiping, Y., Sheng, L., et al. Direct Laser Fabrication of Nickel Slloy Samples. *International Journal of Machine Tools and Manufacture*. **2005**, *45*, 1288-1294. https://doi.org/10.1016/j.ijmachtools.2005.01.014
26. Dinda, G. P., Dasgupta, A. K., Mazumder, J. Texture Control During Laser Deposition of Nickel-based Superalloy. *Scripta Materialia*. **2012**, *67*, 503-506. https://doi.org/10.1016/j.scriptamat.2012.06.014
27. Tabernero, I., Lamikiz, A., Martínez, S., et al. Evaluation of the Mechanical Properties of Inconel 718 Components Built by Laser cladding. *International Journal of Machine Tools & Manufacture*. **2011**, *51*, 465-470. https://doi.org/10.1016/j.ijmachtools.2011.02.003
28. Acharya, R., Bansal, R., Gambone, J. J., et al. Modeling of Solidification and Microstructure Evolution in the Scanning Laser Epitaxy (SLE) Process for Additive Manufacturing With Nickel-Base Superalloy Powders. *ASME 2013 International Mechanical Engineering Congress and Exposition*. San Diego, California, USA. November 15–21, **2013**. IMECE2013-66807. https://doi.org/10.1115/IMECE2013-66807
29. Doubrovski, Z., Verlinden, J. C., Geraedts, J. M. P. Optimal Design for Additive Manufacturing: Opportunities and Challenges. *ASME 2011 International Design Engineering Technical Conferences and Computers and Information in Engineering Conference*. Washington, DC, USA. August 28–31, **2011**. DETC2011-48131. https://doi.org/10.1115/DETC2011-48131
30. LUO, J. Research of External film cooling Performance of Turbine Blade with Different Internal Cooling Structures. *Northwestern Polytechnical University*. **2014**, 17-37. https://doi.org/10.7666/d.D689502
31. Dong, S. Comprehensive Simulation Design Platform for Turbine Cooling Blades. 1 July **2025**. Available online: http://www.lgsim.com/wllqypzhfzsjpt
32. Moffat, R. J. Describing the Uncertainties in Experimental Results. *Experimental Thermal and Fluid Science*. **1988**, *1*, 3-17. https://doi.org/10.1016/0894-1777(88)90043-X
33. Walters, D. K., Leylek, J. H. Impact of Film-Cooling Jets on Turbine Aerodynamic Losses. *Journal of Turbomachinery*. **1999**, *122*, 537-545. https://doi.org/10.1115/1.1303818
34. Na, S., Zhu, B., Bryden, M., et al. CFD Analysis of Film Cooling. *44th AIAA Aerospace Sciences Meeting and Exhibit*. Reno, Nevada. January, 9-12, **2006**. AIAA 2006-22. https://doi.org/10.2514/6.2006-22